RESEARCH ARTICLE

CARBON ENERGY WILEY

Micro/nano-wrinkled elastomeric electrodes enabling high energy storage performance and various form factors

Changeun Yoo[1] | **Seokmin Lee[1]** | **Yongkwon Song[1]** | **Woojae Chang[1]** | **Moon Kyu Park[1]** | **Younji Ko[1]** | **Jinhan Cho[1,2,3]**

[1]Department of Chemical and Biological Engineering, Korea University, Seoul, Seongbuk-gu, Republic of Korea

[2]KU-KIST Graduate School of Converging Science and Technology, Korea University, Seoul, Seongbuk-gu, Republic of Korea

[3]Soft Hybrid Materials Research Center, Advanced Materials Research Division, Korea Institute of Science and Technology (KIST), Seongbuk-gu, Seoul, Republic of Korea

Correspondence
Jinhan Cho, Department of Chemical and Biological Engineering, Korea University, 145 Anam-ro, Seongbuk-gu, Seoul 02841, Republic of Korea.
Email: jinhan71@korea.ac.kr

Abstract

Stretchable elastomer-based electrodes are considered promising energy storage electrodes for next-generation wearable/flexible electronics requiring various shape designs. However, these elastomeric electrodes suffer from the limited electrical conductivity of current collectors, low charge storage capacities, poor interfacial interactions between elastomers and conductive/active materials, and lack of shape controllability. In this study, we report hierarchically micro/nano-wrinkle-structured elastomeric electrodes with notably high energy storage performance and good mechanical/electrochemical stabilities, simultaneously allowing various form factors. For this study, a swelling/deswelling-involved metal nanoparticle (NP) assembly is first performed on thiol-functionalized polydimethylsiloxane (PDMS) elastomers, generating a micro-wrinkled structure and a conductive seed layer for subsequent electrodeposition. After the assembly of metal NPs, the conformal electrodeposition of Ni and NiCo layered double hydroxides layers with a homogeneous nanostructure on the micro-wrinkled PDMS induces the formation of a micro/nano-wrinkled surface morphology with a large active surface area and high electrical conductivity. Based on this unique approach, the formed elastomeric electrodes show higher areal capacity and superior rate capability than conventional elastomeric electrodes while maintaining their electrical/electrochemical properties under external mechanical deformation. This notable mechanical/electrochemical performance can be further enhanced by using spiral-structured PDMS (stretchability of ~500%) and porous-structured PDMS (areal capacity of ~280 $\mu Ah\,cm^{-2}$).

KEYWORDS
elastomeric electrodes, electrodeposition, micro/nano-wrinkled structures

Changeun Yoo, Seokmin Lee and Yongkwon Song contributed equally to this study.

1 | INTRODUCTION

The explosive growth and evolution of wearable/flexible electronics have considerably increased the demands for the development of energy storage devices that can simultaneously yield high energy/power densities, excellent mechanical properties, and desired shape designs.[1–6] Among various energy storage devices, supercapacitors are characterized by a relatively higher power density (or more rapid charging/discharging rates), long-term operational stability, and simpler device structures compared with other devices, because of which supercapacitors are considered promising candidates for next-generation power sources.[7–9] However, despite these notable advantages, the low charge storage capacities of active components for supercapacitors have been critical obstacles to further improvement in their energy densities.[10,11] Additionally, since the practical use of supercapacitors for wearable/flexible electronics requires mechanically stable electrodes with arbitrarily shaped and/or complex geometries, it is highly desirable to develop more elastic and deformable current collector-based electrodes using a facile approach that can be applied to various shapes and sizes of electrodes.

For this purpose, substantial efforts have been focused on the preparation of current collectors using elastic polymers (elastomers) with high mechanical properties.[12,13] Specifically, several approaches (e.g., the incorporation of conductive fillers with high aspect ratio and chemical reduction of metal precursors) have been attempted to achieve elastomeric current collectors (ECCs) with desirable electrical and mechanical properties.[14–18] However, to our knowledge, the formed ECCs have limitations in terms of achievement of high electrical conductivity ($<4000\,S\,cm^{-1}$) and further maintenance of their electrical properties under external mechanical stimuli (such as stretching and bending), despite the incorporation of large amounts of conductive fillers into elastomers.[19–23] These phenomena are mainly caused by the numerous contact resistance sites between adjacent conductive fillers (particularly metal nanowires) and the intrinsically low electrical conductivity of fillers (particularly carbon-based materials and/or conducting polymers).[24,25] Additionally, when preparing energy storage electrodes based on the ECCs, poor interfacial interactions between elastomers and conductive/active materials considerably restrict the stable and uniform deposition of electrode components, adversely affecting the overall mechanical/electrochemical performance of electrodes.[26,27] For example, in the case of use of polydimethylsiloxane (PDMS) elastomers with hydrophobic surface properties, it is very difficult to homogeneously introduce conductive and active components into the exterior and/or interior of PDMS (or porous PDMS) due to their unfavorable interfacial interactions, resulting in the partial aggregation and/or segregation of components.[28] Moreover, such poor interfacial interactions easily lead to structural failures under external mechanical stimuli,[29] which aggravates the overall performance of ECC-based energy storage electrodes. In addition, considering that most ECC-based energy storage electrodes reported to date have primarily used the above-mentioned carbon-based materials (e.g., carbon nanotubes [CNTs]) and/or conducting polymers (e.g., polyaniline [PANI] and polypyrrole [PPy]) as soft active components to ensure the mechanical flexibility,[30–32] their relatively low charge storage capacities act as obstacles to further enhancement of the energy storage performance of elastomeric electrodes.[33,34]

As a promising alternative for improving the mechanical flexibility and energy storage performance of elastomeric electrodes, micro-sized crumpled or wrinkled structures have been introduced into ECC-based energy storage electrodes by the vacuum deposition and/or transfer of electrode layers onto prestrained elastomers in the uniaxial or biaxial direction.[35–38] These unique structures generate a large specific surface area and further allow maintenance of energy storage performance of electrodes by effectively alleviating the mechanical stress that occurs due to externally applied stimuli.[39] However, the above-mentioned vacuum-based approaches have significantly restricted the preparation of wrinkled elastomeric electrodes with various shape designs (such as highly curved and 3D porous structures). Another method for the preparation of wrinkled elastomeric electrodes is the chemical reduction (or electroless deposition) of metal precursors on swollen elastomers.[40,41] However, this chemical reduction generates a nonuniform metal layer with a partially aggregated region, arising from the concentric growth of metal according to the nucleation growth mechanism.[42] Additionally, the nonuniform deposition of the metal layer induces strain localization, resulting in severe cracks and delamination under mechanical deformation. Furthermore, the chemically reduced metal layer shows a relatively low electrical conductivity compared with the electrodeposited metal layer because of large amounts of nonmetallic impurities within the metal layer.

Herein, we introduce hierarchically micro/nano-wrinkle-structured elastomeric energy storage electrodes based on solution-processable metallic ECCs with a large surface area, high electrical conductivity, good

mechanical flexibility, and various shape designs. We highlight that our micro/nano-wrinkled elastomeric electrodes can be prepared using metal nanoparticle (NP) assembly-assisted electrodeposition without additional processes, such as prestraining, thermal annealing, and/or encapsulation. In particular, our solution-based approach can be effectively applied for the preparation of elastomeric electrodes requiring various form factors (spiral, spherical, intaglio-patterned, and 3D porous structures). To the best of our knowledge, solution-processable metallic ECC-based energy storage electrodes have hardly been reported to date; furthermore, the energy storage performance (particularly areal capacity) of the resultant elastomeric electrodes outperforms that of previously reported ones.

For this study, a swelling/deswelling-involved metal NP assembly in organic media is initially performed on thiol-functionalized PDMS (SH-PDMS) elastomers,[43–45] resulting in the formation of a micro-wrinkled structure with a randomly oriented alignment in all directions as well as a conductive seed layer for subsequent electrodeposition (Scheme 1). Based on the formation
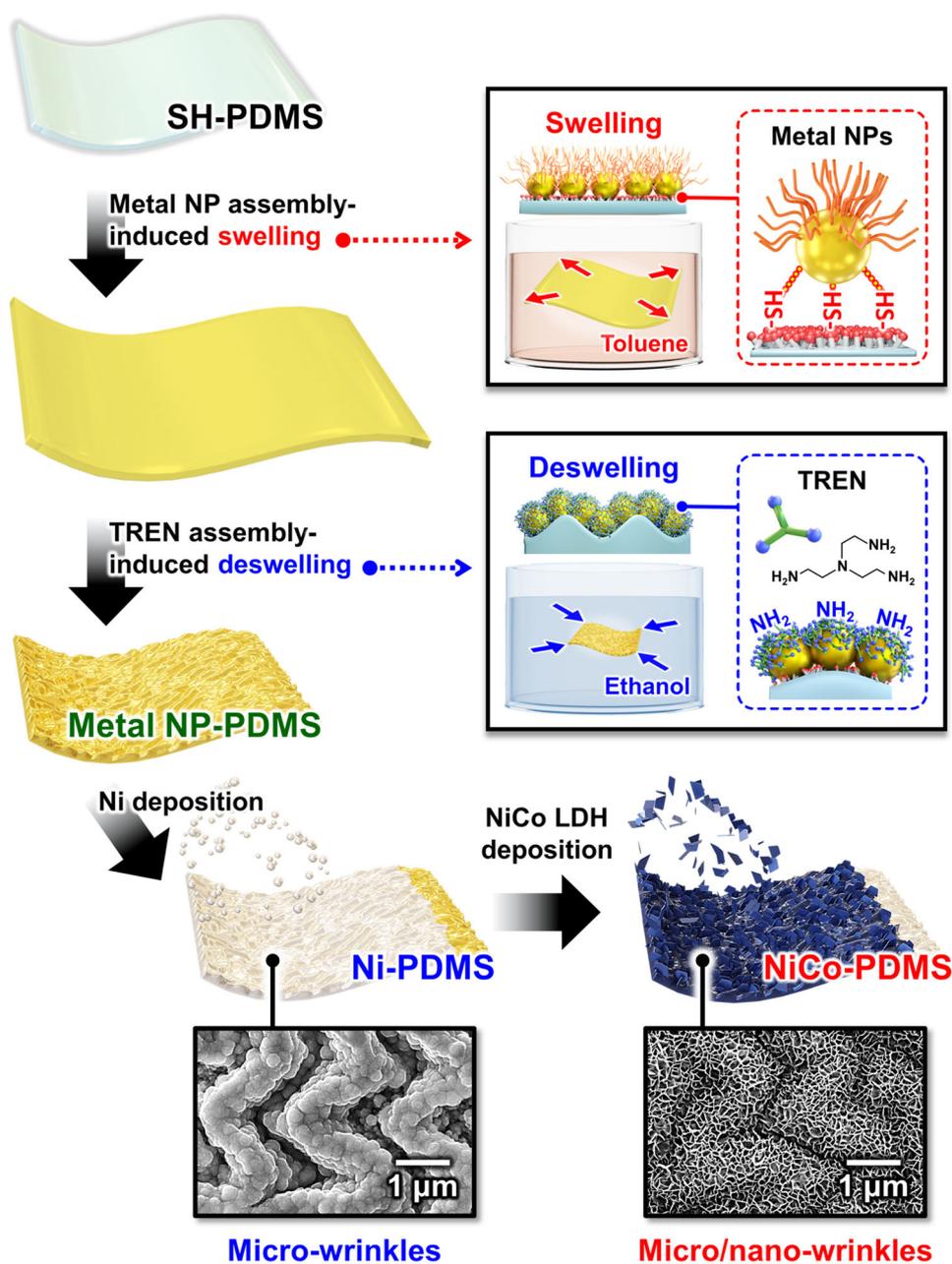
SCHEME 1 Schematic representation of the preparation of hierarchically micro/nano-wrinkled elastomeric energy storage electrodes using metal NP assembly-assisted electrodeposition. LDH, layered double hydroxides; NP, nanoparticle; PDMS, polydimethylsiloxane; TREN, tris(2-aminoethyl)amine.

of a conductive seed layer, Ni can be conformally electrodeposited onto the metal NP-assembled PDMS to prepare ECCs, maintaining their micro-wrinkled structure. As a result, the micro-wrinkled ECCs show a metal-like electrical conductivity of $\sim 1.52 \times 10^4$ S cm^{-1} and stability even under external mechanical stimuli, such as stretching and bending. To realize high-performance metallic ECC-based energy storage electrodes, high-energy NiCo double hydroxides with battery-like capacitive behaviors are further electrodeposited onto the micro-wrinkled ECCs. In this case, the prepared elastomeric electrodes show hierarchically micro/nano-wrinkled structures (i.e., nanostructure by the deposition of a NiCo layered double hydroxides (LDH) layer on the micro-wrinkled structure by metal NP assembly), yielding a high areal capacity ($\sim 34.1\ \mu$Ah cm^{-2} at 0.25 mA cm^{-2}). Importantly, despite the deposition of intrinsically stiff Ni and NiCo metallic layers onto PDMS elastomers, the electrochemical performance of elastomeric electrodes can be substantially maintained even under external mechanical stimuli due to the stress-relaxation effects of the micro/nano-wrinkled structures and the favorable interfacial interactions between electrode components. Additionally, due to the facile shape control of this approach, our elastomeric electrodes with micro/nano-wrinkled structures can achieve an extremely high stretchability of $\sim 500\%$ (by using spiral-structured PDMS) and an extremely high areal capacity of $\sim 280\ \mu$Ah cm^{-2} at 1 mA cm^{-2} (by using porous-structured PDMS). We believe that our approach can provide a basis for developing and designing next-generation energy storage electrodes that can simultaneously meet the requirements of both high mechanical and electrochemical performance.

2 | RESULTS AND DISCUSSION

2.1 | Preparation of ECCs

To develop elastomeric energy storage electrodes, ECCs with large surface area, high electrical conductivity, and excellent mechanical flexibility were preferentially prepared using metal NP assembly and subsequent metal electrodeposition. The metal NP assembly was first performed on SH-PDMS with a thickness of $\sim 500\ \mu$m. In this case, the assembled metal NPs were expected to serve as a conductive seed layer for additional metal electrodeposition. Specifically, tetraoctylammonium bromide-stabilized Au NPs (TOABr-Au NPs) with an average diameter of ~ 8 nm in toluene were densely deposited onto SH-PDMS using strong interfacial interactions (i.e., covalent bonding) between the bare NP surface and SH moieties (Figure S1).[46] That is, the bulky/

insulating and hydrophobic TOABr ligands loosely bound to the surface of Au NPs were effectively removed during the direct adsorption of Au NPs onto SH-PDMS. Additionally, the outermost TOABr ligands existing on the top surface of adsorbed Au NPs could be replaced by the subsequent deposition of small organic molecules with primary amine (NH$_2$) groups (tris(2-aminoethyl) amine [TREN]) in ethanol,[43] as confirmed by Fourier transform infrared spectroscopy (FTIR) (Figure S2). This high interfacial interaction between the NH$_2$ groups of TREN and the surface of Au NPs was also confirmed by the vertical growth of (TOABr-Au NP/TREN)$_n$ multilayers (n: bilayer number), which was observed through UV–vis spectroscopy and a quartz crystal microbalance (QCM) (Figure S3).

Along with the effective removal of TOABr ligands, this metal NP assembly induced a marked change in the surface morphology of PDMS, which was mainly caused by the large difference in the degree of PDMS swelling during successive deposition processes in toluene and ethanol solvents with entirely different polarities (i.e., TOABr-Au NP adsorption in toluene and TREN adsorption in ethanol).[47] Specifically, the TOABr-Au NPs were densely packed onto the swollen SH-PDMS in toluene, while the subsequent adsorption of TREN in ethanol resulted in the significant shrinkage of the swollen TOABr-Au NP-coated PDMS with the outflow of residual toluene within the PDMS (Figure S4A). This swelling/deswelling-involved metal NP assembly led to a strain mismatch between the PDMS elastomer and the densely packed Au NP layer,[48,49] which strongly induced the generation of a micro-wrinkled Au NP layer on the SH-PDMS (Figure S4B). Note that these unique phenomena were not observed from non-swollen elastomers in toluene, such as polyurethane (PU), and an electrostatic interaction-based metal NP assembly in aqueous media (Figure S5).

Due to these structural advantages, the formed (TOABr-Au NP/TREN)$_{n=1}$/PDMS showed an electrical conductivity of $\sim 1.52 \times 10^{-3}$ S cm^{-1}, which markedly increased to ~ 580 S cm^{-1} with further deposition of (TOABr-Au NP/TREN)$_{n=2}$/PDMS (shortly Au NP-PDMS), still maintaining its micro-wrinkled structure with an ~ 110 nm-thick Au NP layer (Figure S6). This rapid improvement in the electrical properties of Au NP-PDMS could be explained by the fact that the aforementioned ligand replacement of bulky/insulating TOABr ligands with small TREN molecules contributed to the enhanced electron transfer by significantly decreasing the separation distance between vertically adjacent Au NP layers (see Figures S1B and S3A).[50] In addition, the TREN layer with hydrophilic properties on the outermost surface enhanced the aqueous interfacial

wettability of Au NP-PDMS, as confirmed from water contact angles (Figure S7), possibly allowing effective metal electrodeposition in aqueous electrolytes.

With the aid of this conductive seed layer, Ni could be successfully electrodeposited with a layer thickness of ~110 nm and a mass loading of ~0.24 mg cm^{-2} onto the Au NP-PDMS, inducing a highly conformal coating on the underlying micro-wrinkled structure, as observed through field-emission scanning electron microscopy (FE-SEM) and energy-dispersive X-ray spectroscopy (EDX) elemental mapping (Figure 1A). In particular, the outermost TREN layer of Au NP-PDMS allowed the stable deposition of metallic Ni layer due to strong interfacial interactions between the NH_2 groups of TREN and the Ni layer.[45] Atomic force microscopy (AFM) revealed that the wavelength (λ) and amplitude (A) of the micro-wrinkled structure of Ni-deposited Au NP-PDMS (shortly Ni-PDMS) were almost identical to those of the initial Au NP-PDMS (λ of ~1.8 μm and A of ~0.4 μm) (Figures 1B and S8). These results implied that the Ni layer was uniformly formed on the conductive Au NP seed layer without any notable distortion of the micro-wrinkled structure. Importantly, when the total surface areas of bare PDMS elastomer and Ni-PDMS were estimated from the AFM measurements, the surface area of micro-wrinkle-structured Ni-PDMS was ~1.4 times higher than that of the bare PDMS elastomer without a wrinkled structure (Figure S9). Additionally, the Ni-PDMS showed a notably high electrical conductivity of ~1.52 × 10^4 S cm^{-1}, indicating the perfect conversion from an insulating PDMS elastomer to a metallic ECC (i.e., Ni-PDMS) that surpassed the reported ECCs in the literature (Figure 1C and Table S1).

Another prominent advantage of our micro-wrinkled Ni-PDMS was that it maintained excellent electrical stability under mechanical deformation. With increasing the tensile strain from 0% to 70%, the resistance change ($\Delta R/R_0$) of Ni-PDMS slightly increased from 0 to ~10.5 (Figure 1D). However, the Ni-PU with a non-wrinkled structure significantly lost its electrical properties even at the relatively low stretched state of over 35%, showing a sudden increase in resistance ($\Delta R/R_0$ of >10^4). Since the Ni-PU was prepared using the same deposition processes (i.e., metal NP assembly and subsequent Ni electrodeposition) as the Ni-PDMS, it was reasonable to conclude that its inferior mechanical properties were a result of the absence of the micro-wrinkled structure due to the non-swollen PU elastomer and the poor interfacial interactions between the PU elastomer and the Au NPs. As more clearly confirmed by FE-SEM (Figure 1E), the Ni-PU showed an obviously irreversibly disconnected and delaminated conductive layer at the stretched state of 70%. On the other hand, the Ni-PDMS, at the same stretched state of 70%, could maintain its electrical pathway despite the partial cracks of the conductive layer and could further recover its interconnected conductive networks after returning to the initial state of 0%. That is, the micro-wrinkled structure of the Ni-PDMS with favorable interfacial interactions between the TREN-coated Au NPs and the Ni layer as well as between the SH-PDMS and the Au NPs could effectively release the mechanical stress occurring at the highly stretched state. Due to these stable mechanical properties, the electrical properties of Ni-PDMS were well maintained even after 5000 stretching cycles at a high tensile strain of 70% (Figure 1F). In addition, the Ni-PDMS showed stable electrical properties in terms of both bending curvature (reaching a bending radius (R) of ~2 mm) and cycling (during 5000 bending cycles at an R of ~2 mm) tests (Figures 1G and S10). Thus, our approach could play a pivotal role in simultaneously realizing high electrical conductivity, mechanical stability, and large surface area of metallic ECCs for the preparation of high-performance energy storage electrodes.

2.2 | Preparation of ECC-based energy storage electrodes

Based on these ECCs (i.e., Ni-PDMS), high-energy NiCo double hydroxides with battery-like capacitive behaviors were further electrodeposited onto the Ni-PDMS for the preparation of ECC-based energy storage electrodes. In this case, the thin NiCo LDH layer with a homogeneous nanostructure was formed on the entire region ranging from the peak to the valley area, which was clearly observed from FE-SEM and EDX elemental mapping images (Figure 2A). That is, the hierarchically micro/nano-wrinkled structures could be formed on the surface of NiCo-deposited Ni-PDMS (shortly NiCo-PDMS), which substantially increased the active surface area (~1.61 m^2 g^{-1}) of the resultant NiCo-PDMS compared with that (~0.64 m^2 g^{-1}) of Ni-PDMS with only a micro-wrinkled structure, as determined by Brunauer–Emmett–Teller (BET) analysis (Figure S11). In particular, considering that the formation of the NiCo LDH layer can significantly contribute to the increase in the active surface area as well as the increase in the electrochemical activity (theoretical capacitance of NiCo LDH ~3000 F g^{-1}),[51] it is quite reasonable to expect that the NiCo-PDMS shows higher energy storage performance than previously reported elastomeric electrodes (*more details are provided in a later section*).

The chemical composition of the NiCo LDH layer of NiCo-PDMS was investigated using X-ray photoelectron
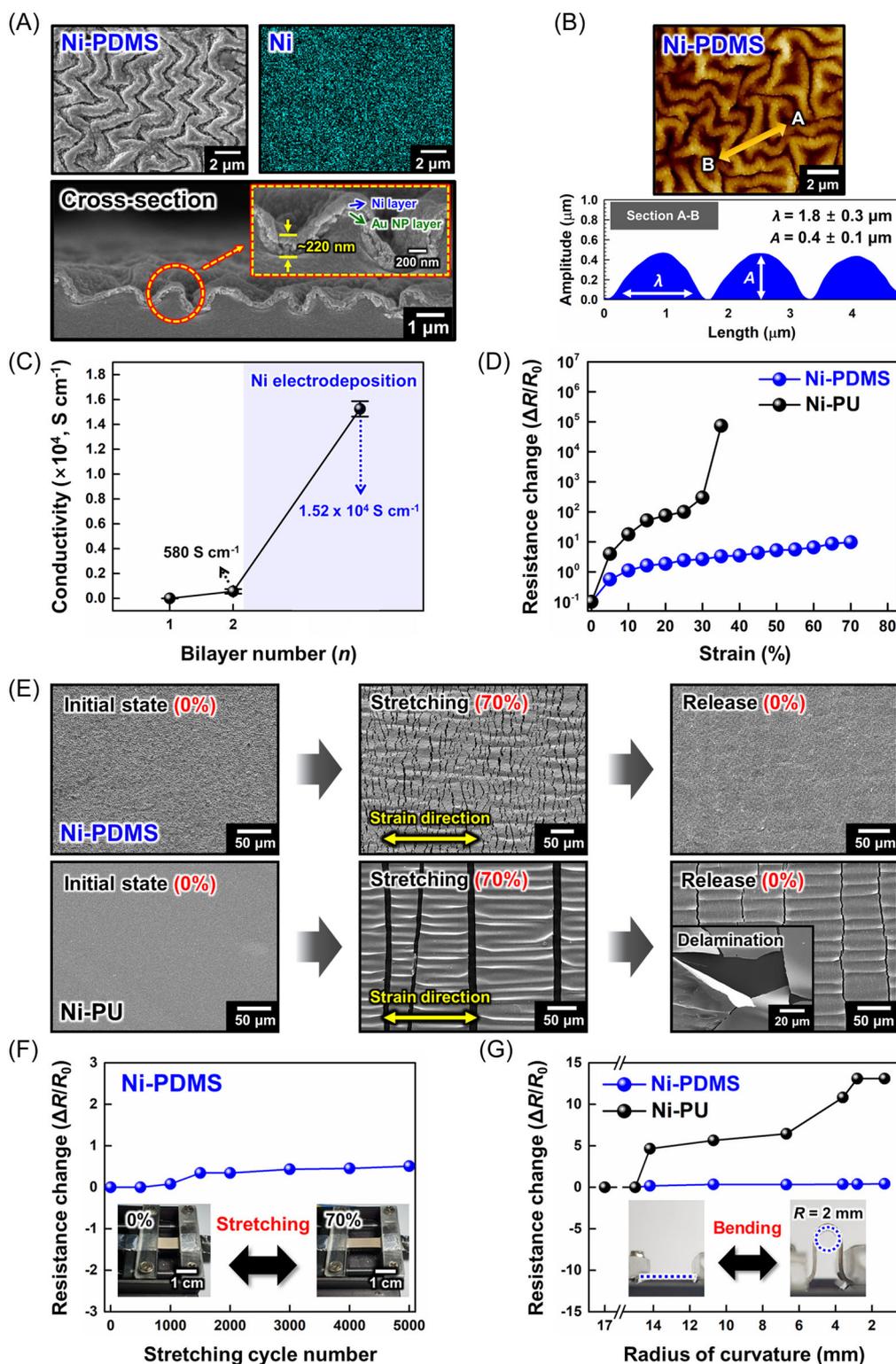
FIGURE 1 (A) Planar FE-SEM (top left side) with EDX elemental mapping (Ni; top right side) and cross-sectional FE-SEM (bottom side) images of Ni-PDMS. The inset in the cross-sectional FE-SEM image shows the deposited Ni and Au NP layers with a total thickness of ~220 nm on the PDMS elastomer. (B) AFM topographic image (scan area = 12.5 μm × 12.5 μm) and cross-sectional height profile of Ni-PDMS. The height profile was obtained from Sections A–B in the AFM image. (C) Electrical conductivity changes of (TOABr-Au NP/TREN)$_n$ with an increase in the bilayer number (n) from 0 to 2 and following Ni electrodeposition on the PDMS elastomer. (D) Resistance changes ($\Delta R/R_0$) of Ni-PDMS and Ni-PU with increasing tensile strain from 0% to 70%. (E) Planar FE-SEM images of Ni-PDMS and Ni-PU at the initial (0%), stretched (70%), and released (0%) states. (F) Resistance changes ($\Delta R/R_0$) and photographs (insets) of Ni-PDMS during 5000 stretching cycles at a tensile strain of 70%. (G) Resistance changes ($\Delta R/R_0$) and photographs (insets) of Ni-PDMS and Ni-PU as a function of bending radius (R).
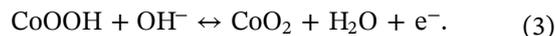
spectroscopy (XPS) (Figure S12). First, the wide-survey XPS spectrum confirmed the existence of Ni, Co, O, and C elements, in which the composition ratio of Ni and Co was measured to be 1:1.4. Additionally, the narrow-survey XPS spectrum of Ni 2p showed double peaks of Ni $2p_{1/2}$ (at 873.4 eV) and Ni $2p_{3/2}$ (at 855.8 eV) with corresponding satellite peaks (at 879.3 and 861.7 eV).[52] In the case of Co 2p, double spin-orbit Co $2p_{1/2}$ and Co $2p_{3/2}$ peaks were detected at 795.7 and 780.1 eV, respectively, which were deconvoluted into Co^{2+} (at 798.5 eV for Co $2p_{1/2}$ and at 781.5 eV for Co $2p_{3/2}$) and Co^{3+} (at 795.6 eV for Co $2p_{1/2}$ and at 779.8 eV for Co $2p_{3/2}$).[53] Moreover, the O 1s peak at 530.5 eV was divided into two different peaks at 530.2 and 531.5 eV associated with metal hydroxyl groups (M-OH) and adsorbed water (H-OH), respectively.[52,53] These results indicated the formation of bimetallic hydroxides (i.e., $Ni(OH)_2$, $Co(OH)_2$, and CoOOH) on the surface of NiCo-PDMS. Furthermore, we examined the crystal structure of the NiCo LDH layer by comparing the X-ray diffraction (XRD) patterns of Ni-PDMS and NiCo-PDMS (Figure S13). In this case, NiCo-PDMS did not show any additional diffraction peak, except for the typical ones (i.e., fcc-Ni, β-$Ni(OH)_2$, and α-$Ni(OH)_2$) associated with the buried Ni layer, directly indicating the amorphous nature of the NiCo LDH layer.[54,55]

It is worth noting here that our solution-based approach is highly advantageous for developing hierarchically micro/nano-wrinkled elastomeric electrodes with arbitrarily shaped or complex geometries, which has not been easily realized using previously reported approaches. As shown in Figure 2B, NiCo-PDMS was successfully prepared into a spiral structure that could overcome the inherent stretching limits of elastomeric matrices, thereby resulting in exceptionally superior stretchability.[56] This spiral NiCo-PDMS showed an almost negligible $\Delta R/R_0$ at the stretched state of 250%, which only slightly increased to ~2.5 despite the extremely high strain of 500% (Figure S14). These results were in stark contrast to those of the flat NiCo-PDMS with a $\Delta R/R_0$ of ~16.7 at a relatively low strain of 50%. In addition, our approach could be effectively applied for the preparation of high-curvature NiCo-PDMS with different micro-patterns and porous NiCo-PDMS (see the Experimental Section of the Supporting Information). Specifically, spherical NiCo-PDMS with an intaglio-patterned structure (micro-pattern size of ~1 μm) and deformable properties was produced, which could maintain its original pattern even after metal NP assembly and Ni/NiCo electrodeposition (Figure 2C). In the case of 3D porous NiCo-PDMS, the entire region ranging from the exterior to the interior of the porous structure was completely and uniformly coated with a NiCo LDH layer without any metal agglomeration and/or

blocking phenomena of pores (Figure 2D). In particular, the hierarchically micro/nano-wrinkled structures could be generated even on the surface of porous NiCo-PDMS, indicating a remarkable enhancement in the energy storage performance of elastomeric electrodes due to the formation of large active surface areas. As a result, we clearly demonstrate that our approach can offer a highly versatile and effective tool for preparing elastomeric electrodes with shape-controlled functionalities, mechanical stress-releasable properties, large active surface area, high electrical conductivity, and/or good mechanical properties.

2.3 | Electrochemical performance of ECC-based energy storage electrodes

To assess the energy storage performance of hierarchically micro/nano-wrinkled NiCo-PDMS, we systematically investigated its electrochemical properties in a three-electrode system using 1 M KOH as an aqueous electrolyte. First, cyclic voltammetry (CV) measurements were conducted in a potential window of 0 to 0.6 V (vs. Hg/HgO) at a scan rate of 30 mV s^{-1} (Figure 3A). In this case, the NiCo-PDMS electrode showed substantially higher current responses than Ni-PDMS and Au NP-PDMS electrodes, implying that the overall capacity of NiCo-PDMS was predominantly governed by the active NiCo LDH layer instead of the buried Ni and/or Au NP layers. Therefore, the conspicuous redox pair in the CV curve of the NiCo-PDMS electrode originated from the battery-like capacitive behaviors of the NiCo LDH layer, which could be described by the reversible conversion reactions of Ni^{2+}/Ni^{3+} and Co^{2+}/Co^{3+} as follows[57,58]:

$$Ni(OH)_2 + OH^- \leftrightarrow NiOOH + H_2O + e^-, \quad (1)$$

$$Co(OH)_2 + OH^- \leftrightarrow CoOOH + H_2O + e^-, \quad (2)$$

$$CoOOH + OH^- \leftrightarrow CoO_2 + H_2O + e^-. \quad (3)$$

When the scan rate increased from 5 to 50 mV s^{-1}, the NiCo-PDMS electrode steadily showed prominent redox pairs without any noticeable deformation of the CV shapes (Figure S15A), indicating good rate capability. Additionally, the almost linear relationship between the square root of scan rates ($v^{1/2}$) and the redox peak current densities (I_p) in the scan rate-dependent CV curves showed diffusion-controlled behaviors during electrochemical sweeps (Figure S15B).[59]

To further elucidate the structural effects of the hierarchically micro/nano-wrinkled structures of the
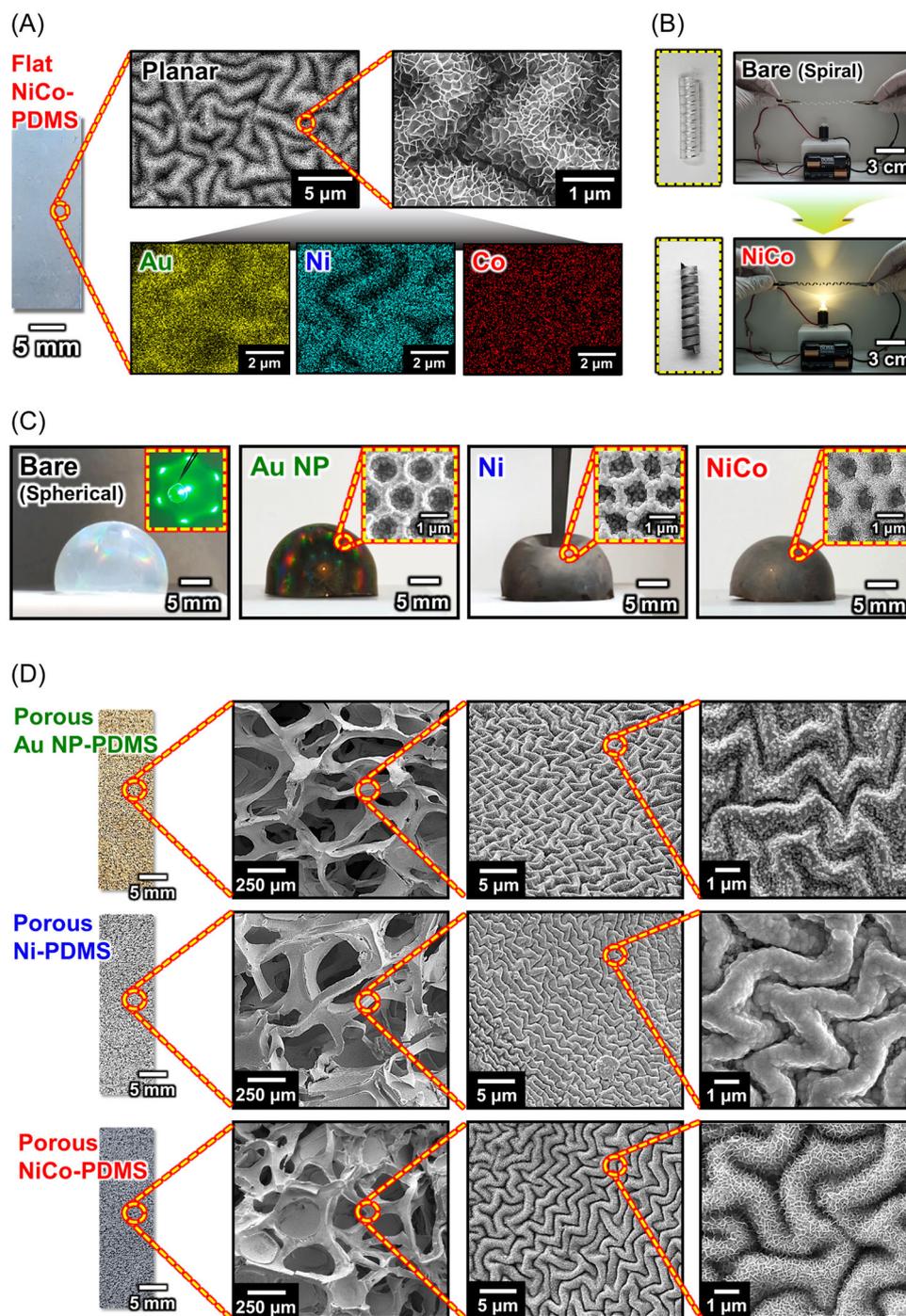
FIGURE 2 (A) Photographs (left side) and planar FE-SEM images (top right side) with EDX elemental mapping (Au, Ni, and Co; bottom right side) of NiCo-PDMS. (B) Photographs of a spiral-structured bare PDMS elastomer and NiCo-PDMS connected with a light-emitting diode (LED) at the stretched state of 500%. (C) Photographs and planar FE-SEM images (insets) of a spherical-structured bare PDMS elastomer, Au NP-PDMS, Ni-PDMS, and NiCo-PDMS with intaglio patterns. The inset in the photograph of the bare PDMS elastomer shows the laser-induced diffraction pattern of the intaglio structure. (D) Photographs (left side) and planar FE-SEM images (right side) of porous-structured Au NP-PDMS, Ni-PDMS, and NiCo-PDMS.

NiCo-PDMS electrode, its electrochemical performance was compared with that of the NiCo-PU electrode prepared using the same experimental procedures. In this case, the surface morphology of NiCo-PU only showed the nanostructure resulting from the formation of a NiCo LDH layer without any micro-wrinkles due to the non-swollen PU elastomer, as mentioned earlier (Figure S16). As shown in Figure 3B, the NiCo-PDMS
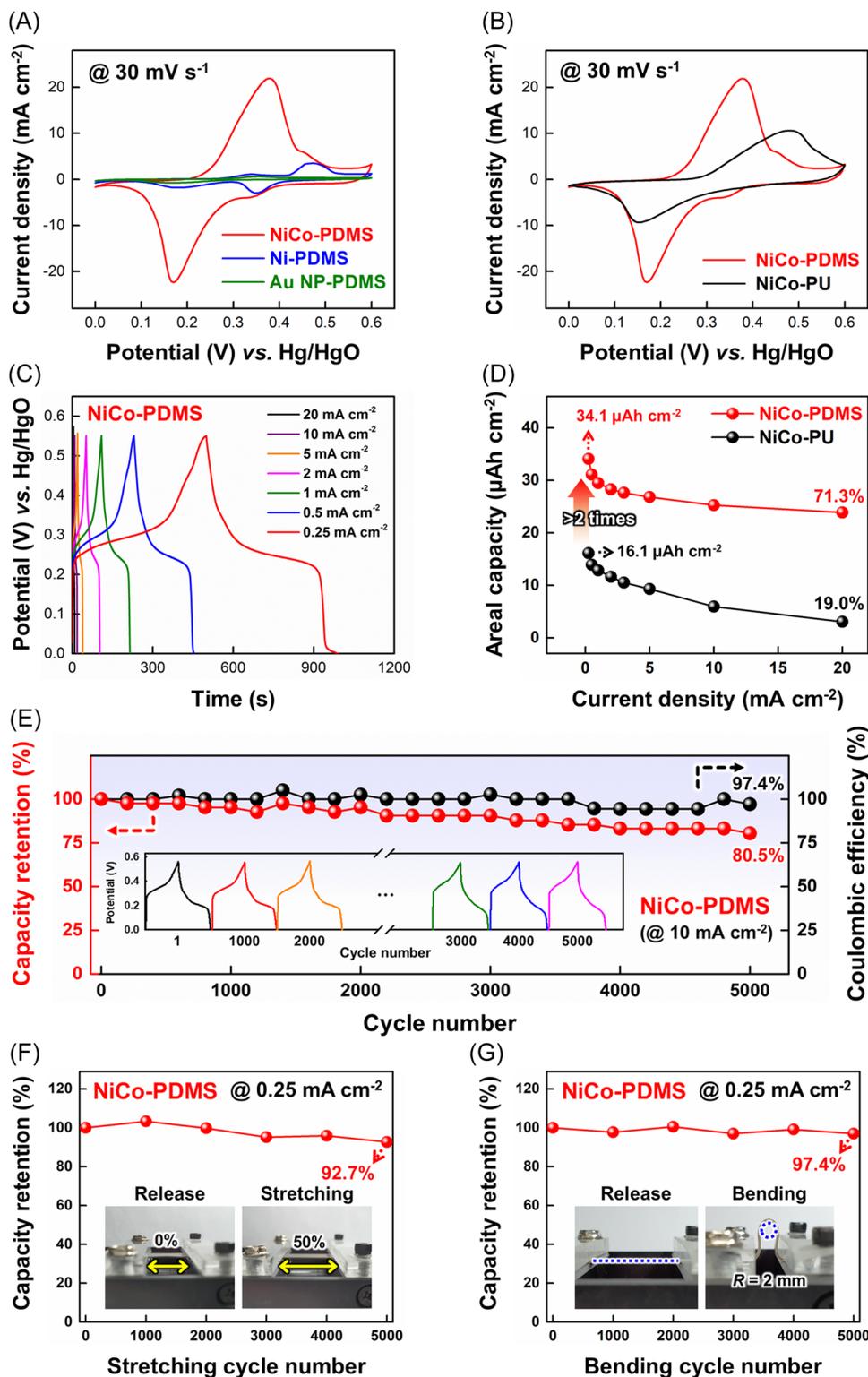
FIGURE 3 (A) Comparison of CV curves between NiCo-PDMS, Ni-PDMS, and Au NP-PDMS electrodes at a scan rate of $30 \, \text{mV s}^{-1}$. (B) Comparison of CV curves between NiCo-PDMS and NiCo-PU electrodes at a scan rate of $30 \, \text{mV s}^{-1}$. (C) GCD profiles of the NiCo-PDMS electrode at varied current densities ranging from 0.25 to $20 \, \text{mA cm}^{-2}$. (D) Comparison of the areal capacity (obtained from GCD curves) between NiCo-PDMS and NiCo-PU electrodes with increasing current density from 0.25 to $20 \, \text{mA cm}^{-2}$. (E) Capacity retention (left axis, red line/circles) and Coulombic efficiency (right axis, black line/circles) of the NiCo-PDMS electrode during 5000 GCD cycles at a current density of $10 \, \text{mA cm}^{-2}$. The inset shows the GCD profiles at cycle numbers of 1, 1000, 2000, 3000, 4000, and 5000. Capacity retention and photographs (insets) of the NiCo-PDMS electrode at a current density of $0.25 \, \text{mA cm}^{-2}$ (F) during 5000 stretching cycles at a tensile strain of 70% and (G) during 5000 bending cycles at a bending radius (R) of $2 \, \text{mm}$.

electrode showed a much larger integrated CV area and smaller peak separation (i.e., redox potential difference (ΔE_p) inversely correlated with charge-transfer rates) than the NiCo-PU electrode at the same scan rate of 30 mV s^{-1}. These phenomena suggested that the micro/nano-wrinkled structures of NiCo-PDMS contributed not only to the large active surface area but also to the rapid charge-transfer rates, which was clear from observations of the surface morphologies of the electrodes after electrochemical sweeps. Specifically, the NiCo-PDMS electrode could stably preserve its well-interconnected charge-transfer networks by effectively alleviating the volume stress generated at the active NiCo LDH layer during electrochemical sweeps through the micro/nano-wrinkled structures and the well-defined interfacial interactions, in significant contrast to the NiCo-PU electrode with numerous cracks (Figure S17).

Based on these electrochemical behaviors, we evaluated the charge storage capability by recording galvanostatic charge/discharge (GCD) profiles by progressively increasing the current density from 0.25 to 20 mA cm^{-2} (Figures 3C and S18). In this case, the GCD profiles revealed the nonlinear charge/discharge curves with plateau regions of battery-like capacitive behaviors of the NiCo LDH layer, corresponding to the CV measurements. When the areal capacity was calculated from the GCD curves, the NiCo-PDMS electrode achieved an areal capacity of ~34.1 µAh cm^{-2} at a low current density of 0.25 mA cm^{-2}, delivering ~71.3% of the initial capacity even at a high current density of 20 mA cm^{-2} (Figure 3D). On the basis of the mass loading of active NiCo LDH layer (~0.11 mg cm^{-2}), the gravimetric capacity of the NiCo-PDMS electrode was measured to be ~310 mAh g^{-1}. Additionally, on calculating the gravimetric capacity from the total mass loading of electrode layer (i.e., the total mass of Au NP, Ni, and NiCo LDH layers ~0.83 mg cm^{-2}), it was estimated to be ~41 mAh g^{-1}. On the other hand, the NiCo-PU electrode showed an areal capacity that was at least two times smaller (~16.1 µAh cm^{-2} at 0.25 mA cm^{-2}), with substantially lower capacity retention (~19.0% at 20 mA cm^{-2}) than the NiCo-PDMS electrode, mainly due to the lower active surface area and the loss of the charge-transfer pathway of the cracked NiCo-PU electrode without any micro-wrinkles, as mentioned above. That is, the formation of micro/nano-wrinkled structures on the NiCo-PDMS electrode led to the high areal capacity and superior rate capability based on its large active surface area and well-interconnected conductive networks. The NiCo-PDMS electrode also showed excellent long-term operational stability with a capacity retention of ~80.5% and a Coulombic efficiency of ~97.4% after 5000 GCD cycles at a current density of 10 mA cm^{-2} without any notable

structural failure (Figures 3E and S19), implying the formation of robust micro/nano-wrinkled structures.

Along with the evaluation of electrochemical performance, the mechanical stability of the NiCo-PDMS electrode was studied by measuring the capacity (calculated from GCD curves at 0.25 mA cm^{-2}) under repeated mechanical stimuli conditions. First, the capacity was recorded every 1000 cycles, accompanied by stretching (at a tensile strain of 50%) and relaxation. After 5000 stretching cycles, the NiCo-PDMS electrode maintained ~92.7% of its initial capacity without any significant change in the GCD shapes (Figures 3F and S20A). Electrochemical impedance spectroscopy (EIS) analysis showed a negligible change in the resistance behaviors with facile charge-transfer kinetics after 5000 stretching cycles (Figure S20B). Additionally, the outstanding mechanical properties of the NiCo-PDMS electrode were also confirmed during 5000 bending cycles at an R of ~2 mm, achieving a capacity retention of ~97.4% with almost unchanged electrochemical behaviors (Figures 3G and S21). These results clearly proved that the hierarchically micro/nano-wrinkled structures could efficiently release the mechanical stress, and thereby, NiCo-PDMS could be considered a promising candidate for stretchable and flexible energy storage electrodes with high performance features.

2.4 | Electrochemical performance of spiral-structured energy storage electrodes

Another important advantage of our approach was that various shape-structured elastomers could be easily converted into energy storage electrodes. Based on this facile shape control, we attempted to further enhance the mechanical properties by using a spiral-structured design in the NiCo-PDMS (Figures 4A and 2B). As mentioned earlier, the spiral NiCo-PDMS could show remarkably improved electrical stability (or stretchability) by effectively diminishing the tensile strain due to its spiral structure and hierarchically micro/nano-wrinkled structures. To more evidently demonstrate the effectiveness of the spiral structure, we further investigated the electrochemical stability of the spiral NiCo-PDMS electrode under an extremely high tensile strain of 500%. As shown in Figure 4B, the spiral NiCo-PDMS electrode showed only a 4% decrease in the integrated CV area with an obvious redox pair at the stretched state; however, the peak separation (ΔE_p) between redox peaks increased to some degree due to the increased resistance values. These resistance behaviors were supported by the EIS measurements, in which the stretched spiral electrode showed a higher equivalent series resistance (R_s of
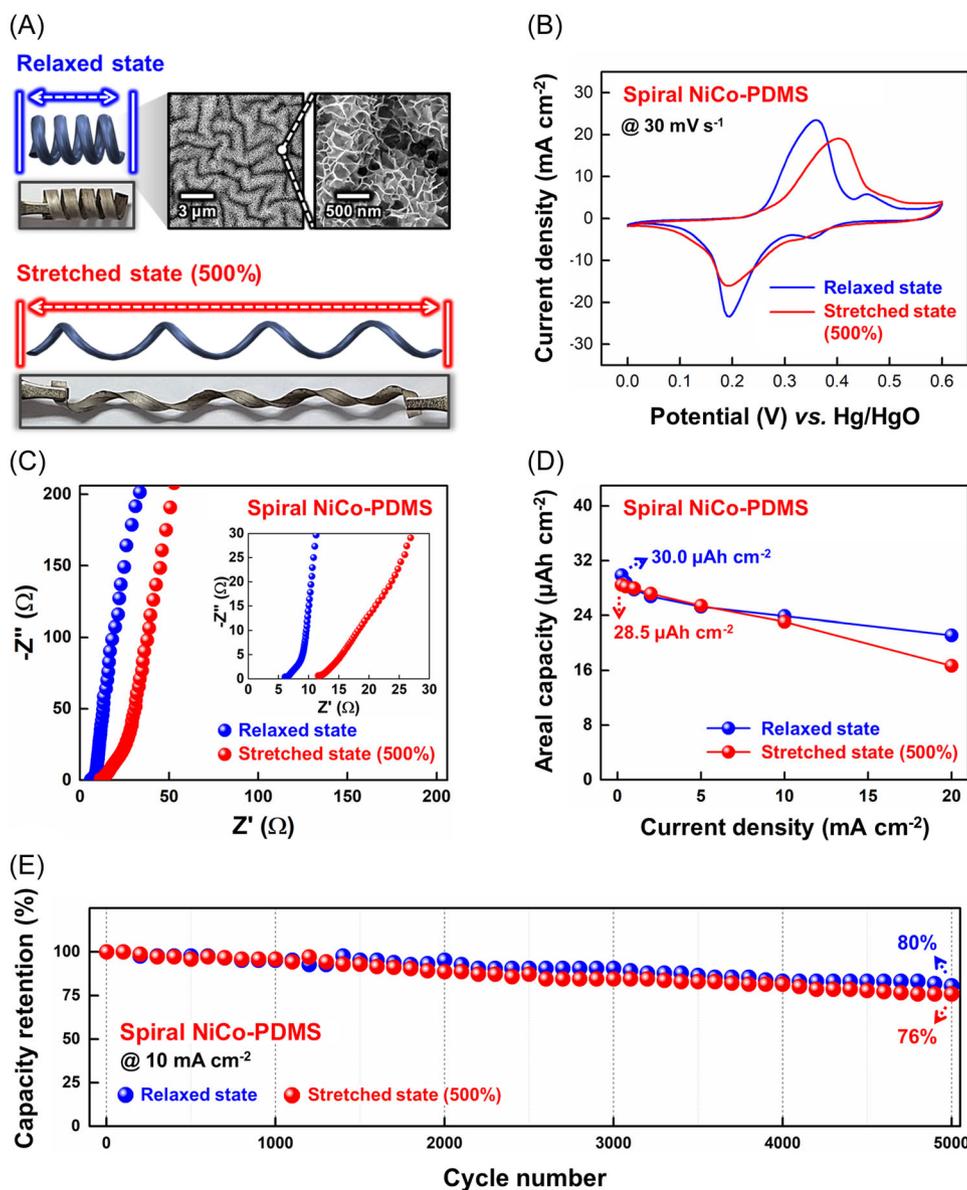
FIGURE 4 (A) Schematic illustration and photographs of spiral NiCo-PDMS at the relaxed (0%; top left side) and stretched (500%; bottom side) states. The planar FE-SEM images of spiral NiCo-PDMS at the relaxed state are also shown (top right side). Comparison of (B) CV curves at a scan rate of 30 mV s^{-1}, (C) Nyquist plots, (D) areal capacity (obtained from GCD curves at different current densities ranging from 0.25 to 20 mA cm^{-2}), and (E) long-term cycling stability (during 5000 GCD cycles at a current density of 10 mA cm^{-2}) of the spiral NiCo-PDMS electrode between the relaxed (0%) and stretched (500%) states.

~11.6 Ω) and charge-transfer resistance (R_{ct}; determined by the semicircles in the high-frequency region) than those of the relaxed electrode (R_s of ~6.1 Ω) (Figure 4C). In particular, these phenomena were quite consistent with the aforementioned results of electrical stability with a $\Delta R/R_0$ of ~2.5 at the same tensile strain of 500% (Figure S14). Additionally, the spiral NiCo-PDMS electrode showed no significant difference in the ion diffusion resistance (or Warburg impedance [W], determined by the slopes of the tails in the low-frequency region) between the stretched and relaxed states.

Based on these enhanced mechanical properties, the spiral NiCo-PDMS electrode could be stably operated even at the stretched state of 500%, which was clearly confirmed by the scan rate-dependent CV curves (from 5 to 50 mV s^{-1}) and current density-dependent GCD profiles (from 0.25 to 20 mA cm^{-2}) (Figure S22). Additionally, the areal capacity obtained from the GCD profiles at the stretched state was maintained nearly the same as that at the relaxed state and only slightly decreased at a high current density of 20 mA cm^{-2} (Figure 4D). To further investigate both the mechanical

and operational stabilities of the spiral NiCo-PDMS electrode, we compared the cycling retention at the stretched and relaxed states during 5000 GCD cycles at a current density of 10 mA cm^{-2} (Figure 4E). In this case, even at the stretched state of 500%, the spiral electrode retained ~76% of the initial capacity after 5000 GCD cycles, which was quite comparable to the relaxed state with a capacity retention of ~80%. These results showed that a spiral-structured energy storage electrode with remarkably enhanced mechanical features could be easily realized using our unique approach.

2.5 | Electrochemical performance of 3D porous-structured energy storage electrodes

Due to its facile shape control on elastomeric electrodes, a 3D porous-structured NiCo-PDMS electrode (elastomer thickness of ~1 mm) with mechanical deformability was prepared, as shown in Figures 5A,B and 2D. The porous structure could notably increase the active surface area along with hierarchically micro/nano-wrinkled structures, thereby inducing a marked increase in the energy storage performance (particularly areal capacity) of electrodes. To quantify this enlarged surface area, the electrochemical surface area (ECSA) was estimated from the double-layer capacitance (C_{dl}) acquired at different scan rates of CV curves in the non-Faradaic potential region from 0 to 0.1 V (Figures 5C and S23).[60] As a result, the ECSA of the porous NiCo-PDMS electrode was nearly nine times larger than that of the flat NiCo-PDMS electrode, apparently demonstrating that the porous structure could remarkably increase the active surface area of the electrode. Therefore, we increased the concentration of the KOH electrolyte from 1 to 6 M due to the large difference in the active surface area between porous NiCo-PDMS and flat NiCo-PDMS electrodes. Additionally, the porous NiCo-PDMS electrode showed complete wettability to the aqueous electrolyte, which was in sharp contrast to the bare porous PDMS elastomer with hydrophobic surface properties (Figure S24). That is, the conformal coating of a hydrophilic NiCo LDH layer from the exterior to the interior of the porous PDMS elastomer allowed effective penetration of the electrolyte into the porous structure for facile ion transportation.

As shown in Figure 5D, the porous NiCo-PDMS electrode showed significantly better current responses and integrated CV area than the flat NiCo-PDMS electrode at a scan rate of 30 mV s^{-1}. However, the redox peaks of the porous electrode were slightly deviated and broadened compared with those of the flat electrode, as

also observed in the scan rate-dependent CV curves ranging from 5 to 50 mV s^{-1} (Figures 3D and S25). These trends were further intensified as the mass loading of the active NiCo LDH layer increased (Figure S26), which was mainly caused by the increased internal resistance.[61] As evidence of these phenomena, the EIS analysis showed that the porous electrode had a higher R_s of ~4.5 Ω with increased ion diffusion resistance (from the lower slope of the tail) than the flat electrode with an R_s of ~2.9 Ω (Figure 5E). Despite the slight increase in the resistance values, the porous NiCo-PDMS electrode could achieve an extremely high areal capacity of ~280 μAh cm^{-2} at a current density of 1 mA cm^{-2}, which substantially outperformed that of the flat NiCo-PDMS electrode and previously reported elastomeric electrodes (Figure 5F and Table S2). In this case, it was worth noting that this markedly enhanced capacity value originated from the enlarged active surface area by the optimal formation of a hierarchical structure composed of micro/nano-wrinkles on the macroporous framework. The porous NiCo-PDMS electrode also showed good rate capability with a capacity retention of ~72.1% (areal capacity of ~202 μAh cm^{-2}), even at a high current density of 20 mA cm^{-2}. The electrochemical stability was also examined during 5000 GCD cycles at a current density of 20 mA cm^{-2}, showing a satisfactory cycling retention of ~81.3% with a Coulombic efficiency of ~97.4% (Figure 5G). These results clearly proved that our unique metal NP assembly-assisted electrodeposition could enable the preparation of a fine and robust hierarchical structure using favorable interfacial interactions and further provide an efficient pathway for developing and designing high-performance energy storage electrodes with various form factors.

To further demonstrate the practicality of our elastomeric electrodes, we constructed an asymmetric energy storage device with porous NiCo-PDMS as a positive electrode and carbon textile (CT) as a negative electrode using a 6 M KOH electrolyte. In this case, the negative CT electrode showed the electric double-layer capacitor (EDLC) behaviors of rectangular-shaped CV and triangular-shaped GCD curves in a three-electrode system with a potential window of −1.0 to 0 V (vs. Hg/HgO) (Figure S27). Therefore, by controlling the charge balance of the two electrodes, the overall potential window of the full-cell device (shortly porous NiCo-PDMS//CT) could be successfully increased to 1.6 V with no apparent overpotential region (Figures S28A and S28B). As a result, the as-prepared porous NiCo-PDMS//CT showed stable operation with mixed capacitive features of EDLC and Faradaic reactions in the potential window of 1.6 V, as confirmed by the scan rate-dependent CV (from 5 to 50 mV s^{-1}) and current density-dependent GCD (from 1 to 20 mA cm^{-2}) profiles (Figures S28C and S28D). The areal
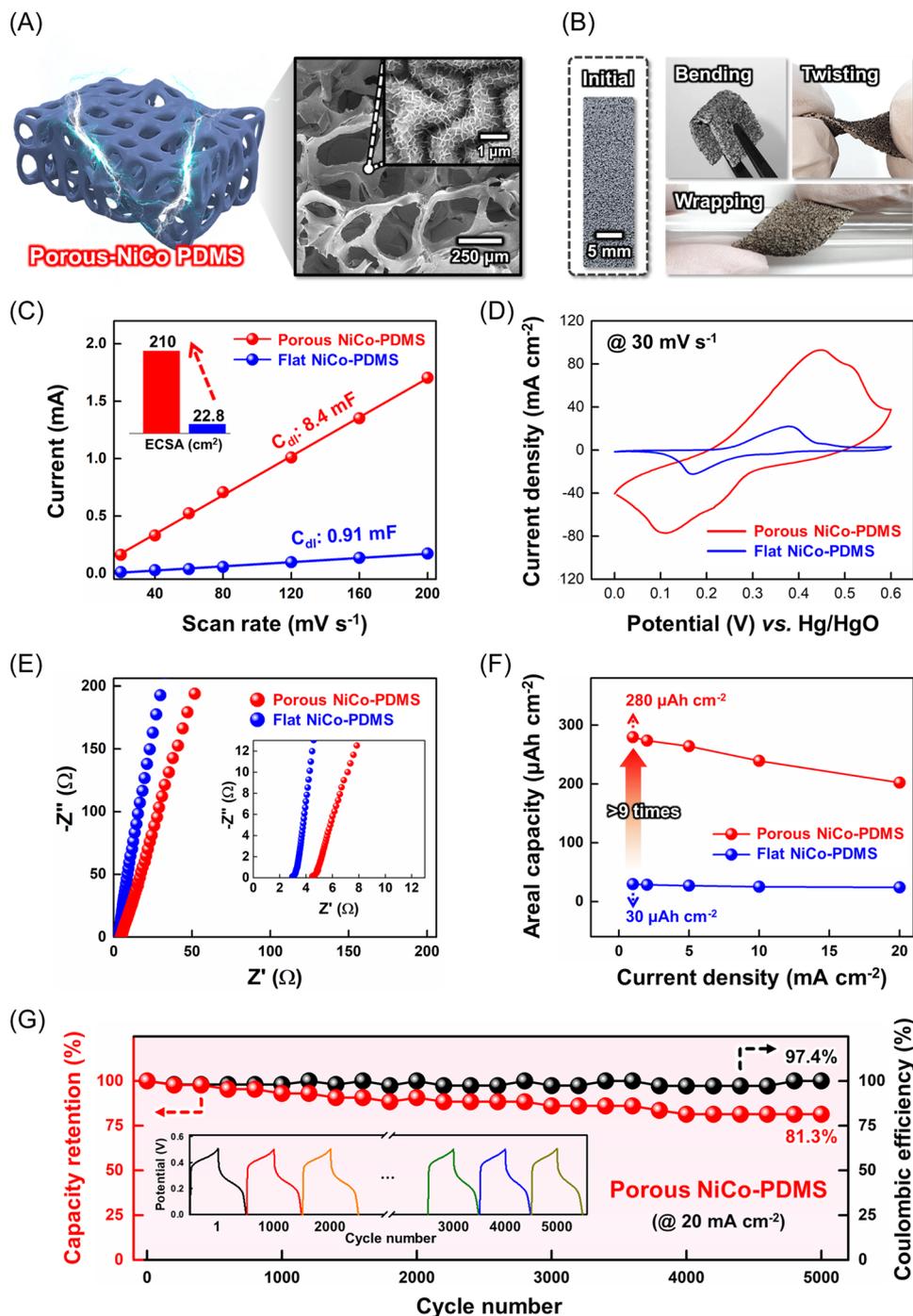
FIGURE 5 (A) Schematic illustration and planar FE-SEM images of porous NiCo-PDMS. (B) Photographs of porous NiCo-PDMS at the initial state (left side) and under various mechanical deformation states (bending, twisting, and wrapping; right side). (C) Comparison of the current versus scan rate plots between porous NiCo-PDMS and flat NiCo-PDMS electrodes from the CV curves at various scan rates ranging from 5 to 200 mV s^{-1} in the non-Faradaic potential window from 0 to 0.1 V. In this case, the double-layer capacitance (C_{dl}; obtained from the slope of linearly fitted lines) and corresponding ECSA values are also shown. Comparison of (D) CV curves at a scan rate of 30 mV s^{-1}, (E) Nyquist plots, and (F) areal capacity (obtained from GCD curves at different current densities ranging from 1 to 20 mA cm^{-2}) between porous NiCo-PDMS and flat NiCo-PDMS electrodes. (G) Capacity retention (left axis, red line/circles) and Coulombic efficiency (right axis, black line/circles) of the porous NiCo-PDMS electrode during 5000 GCD cycles at a current density of 20 mA cm^{-2}. The inset shows the GCD profiles at cycle numbers 1, 1000, 2000, 3000, 4000, and 5000.

capacity of porous NiCo-PDMS//CT was measured to be ~331 μAh cm^{-2} at a current density of 1 mA cm^{-2}, showing a capacity retention of ~63.2% at a current density of 20 mA cm^{-2} (Figure S28E). In addition, the maximum areal energy and power densities were calculated to be approximately 264.6 μWh cm^{-2} (at 1 mA cm^{-2}) and 16.0 mW cm^{-2} (at 20 mA cm^{-2}), respectively. When the operational stability was evaluated by the GCD measurements at a current density of 20 mA cm^{-2} for 5000 cycles, the porous NiCo-PDMS//CT retained ~74.0% of the initial capacity with a high Coulombic efficiency of ~98.5% (Figure S28F). By considering these outperforming performance indicators based on the micro/nano-wrinkled structure and shape controllability of elastomeric electrodes, we strongly believe that our approach has excellent potential for the use toward the development of high-performance stretchable/flexible energy storage devices.

3 | CONCLUSION

In this study, we demonstrated that hierarchically micro/nano-wrinkle-structured elastomeric energy storage electrodes with unprecedentedly high areal capacity, good rate capability, excellent mechanical properties, and facile shape control could be prepared through metal NP assembly and subsequent Ni/NiCo electrodeposition. Our approach was characterized by the fact that the assembly of a densely packed metal NP layer onto swollen SH-PDMS and the subsequent electrodeposition of conductive/active metallic layers could induce the formation of micro/nano-wrinkled structures with stable interfacial interactions, which could significantly contribute to the large active surface area, high electrical conductivity, and effective alleviation of mechanical stress under external deformation. In particular, when our approach was applied to spiral- and porous-structured PDMS elastomers, micro/nano-wrinkled structures were conformally formed on the surface of those PDMS elastomers regardless of their arbitrarily shaped design. As a result, the formed electrodes showed an extremely high stretchability of ~500% (by using spiral-structured PDMS) and an areal capacity of ~280 μAh cm^{-2} (by using porous-structured PDMS), along with superior rate capability and good mechanical flexibility, which outperformed conventional elastomeric energy storage electrodes. Considering that the elastomeric electrodes reported to date have many difficulties in satisfying both high energy storage and good mechnical performance, our approach could provide a breakthrough for developing and designing high-performance elastomeric energy storage electrodes with desired shapes.

CONFLICT OF INTEREST STATEMENT

The authors declare no conflicts of interest.

ORCID

Changeun Yoo https://orcid.org/0000-0001-7894-6371
Yongkwon Song https://orcid.org/0000-0002-2173-8157
Jinhan Cho https://orcid.org/0000-0002-7097-5968

REFERENCES

1. Simon P, Gogotsi Y. Perspectives for electrochemical capacitors and related devices. *Nat Mater*. 2020;19(8):1151-1163.
2. Pomerantseva E, Bonaccorso F, Feng X, Cui Y, Gogotsi Y. Energy storage: the future enabled by nanomaterials. *Science*. 2019;366(6468):969.
3. Li H, Tang Z, Liu Z, Zhi C. Evaluating flexibility and wearability of flexible energy storage devices. *Joule*. 2019;3(3):613-619.
4. Zhao Z, Xia K, Hou Y, Zhang Q, Ye Z, Lu J. Designing flexible, smart and self-sustainable supercapacitors for portable/wearable electronics: from conductive polymers. *Chem Soc Rev*. 2021;50(22):12702-12743.
5. Rogers JA, Someya T, Huang Y. Materials and mechanics for stretchable electronics. *Science*. 2010;327(5973):1603-1607.
6. Li L, Wu Z, Yuan S, Zhang XB. Advances and challenges for flexible energy storage and conversion devices and systems. *Energy Environ Sci*. 2014;7(7):2101-2122.
7. Hongtao S, Jian Z, Daniel B, et al. Hierarchical 3D electrodes for electrochemical energy storage. *Nat Rev Mater*. 2019;4(12):45-60.
8. Gogotsi Y, Simon P. True performance metrics in electrochemical energy storage. *Science*. 2011;334(6058):917-918.
9. Shao Y, El-Kady MF, Sun J, et al. Design and mechanisms of asymmetric supercapacitors. *Chem Rev*. 2018;118(18):9233-9280.
10. Aricò AS, Bruce P, Scrosati B, Tarascon JM, van Schalkwijk W. Nanostructured materials for advanced energy conversion and storage devices. *Nat Mater*. 2005;4(5):366-377.
11. Keum K, Kim JW, Hong SY, Son JG, Lee SS, Ha JS. Flexible stretchable supercapacitors with novel functionality for wearable electronics. *Adv Mater*. 2020;32(51):2002180.
12. Mackanic DG, Chang TH, Huang Z, Cui Y, Bao Z. Stretchable electrochemical energy storage devices. *Chem Soc Rev*. 2020;49(13):4466-4495.
13. Mu H, Wang W, Yang L, et al. Fully integrated design of intrinsically stretchable electrodes for stretchable supercapacitors. *Energy Storage Mater*. 2021;39:130-138.
14. Mu H, Huang X, Wang W, Tian X, An Z, Wang G. High-performance-integrated stretchable supercapacitors based on a

polyurethane organo/hydrogel electrolyte. *ACS Appl Mater Interfaces*. 2022;14(1):622-632.

15. Li Z, Hu K, Yang M, et al. Elastic Cu@PPy sponge for hybrid device with energy conversion and storage. *Nano Energy*. 2019;58:852-861.

16. Chen X, Huang H, Pan L, Liu T, Niederberger M. Fully integrated design of a stretchable solid-state lithium-ion full battery. *Adv Mater*. 2019;31(43):1904648.

17. Wang X, Yang C, Jin J, Li X, Cheng Q, Wang G. High-performance stretchable supercapacitors based on intrinsically stretchable acrylate rubber/MWCNTs@conductive polymer composite electrodes. *J Mater Chem A*. 2018;6(10):4432-4442.

18. Yun TG, Park M, Kim DH, et al. All-transparent stretchable electrochromic supercapacitor wearable patch device. *ACS Nano*. 2019;13(3):3141-3150.

19. Cai G, Park S, Cheng X, Eh ALS, Lee PS. Inkjet-printed metal oxide nanoparticles on elastomer for strain-adaptive transmissive electrochromic energy storage systems. *Sci Technol Adv Mater*. 2018;19(1):759-770.

20. Park S, Thangavel G, Parida K, Li S, Lee PS. A stretchable and self-healing energy storage device based on mechanically and electrically restorative Liquid-Metal particles and carboxylated polyurethane composites. *Adv Mater*. 2019;31(1):1805536.

21. Yu J, Lu W, Pei S, et al. Omnidirectionally stretchable high-performance supercapacitor based on isotropic buckled carbon nanotube films. *ACS Nano*. 2016;10(5):5204-5211.

22. Liu HS, Pan BC, Liou GS. Highly transparent Ag NW/PDMS stretchable electrodes for elastomeric electrochromic devices. *Nanoscale*. 2017;9(7):2633-2639.

23. Song WJ, Park J, Kim DH, et al. Jabuticaba-inspired hybrid carbon filler/polymer electrode for use in highly stretchable aqueous Li-ion batteries. *Adv Energy Mater*. 2018;8(10):1702478.

24. Kim DC, Shim HJ, Lee W, Koo JH, Kim DH. Material-based approaches for the fabrication of stretchable electronics. *Adv Mater*. 2020;32(15):1902743.

25. Amjadi M, Pichitpajongkit A, Lee S, Ryu S, Park I. Highly stretchable and sensitive strain sensor based on silver nanowire-elastomer nanocomposite. *ACS Nano*. 2014;8(5):5154-5163.

26. Zhou A, Sim R, Luo Y, Gao X. High-performance stretchable electrodes prepared from elastomeric current collectors and binders. *J Mater Chem A*. 2017;5(40):21550-21559.

27. Lamberti A, Clerici F, Fontana M, Scaltrito L. A highly stretchable supercapacitor using laser-induced graphene electrodes onto elastomeric substrate. *Adv Energy Mater*. 2016;6(10):1600050.

28. Liu W, Chen Z, Zhou G, et al. 3D porous sponge-inspired electrode for stretchable lithium-ion batteries. *Adv Mater*. 2016;28(18):3578-3583.

29. Moon IK, Ki B, Oh J. Three-dimensional porous stretchable supercapacitor with wavy structured PEDOT:PSS/graphene electrode. *Chem Eng J*. 2020;392:123794.

30. Li L, Wang L, Ye T, Peng H, Zhang Y. Stretchable energy storage devices based on carbon materials. *Small*. 2021;17(48):2005015.

31. Kumar R, Joanni E, Sahoo S, et al. An overview of recent progress in nanostructured carbon-based supercapacitor electrodes: from zero to bi-dimensional materials. *Carbon*. 2022;193:298-338.

32. Zhong M, Zhang M, Li X. Carbon nanomaterials and their composites for supercapacitors. *Carbon Energy*. 2022;4(5):950-985.

33. Swain N, Tripathy A, Thirumurugan A, Saravanakumar B, Schmidt-Mende L, Ramadoss A. A brief review on stretchable, compressible, and deformable supercapacitor for smart devices. *Chem Eng J*. 2022;446:136876.

34. Zhang LL, Zhao XS. Carbon-based materials as supercapacitor electrodes. *Chem Soc Rev*. 2009;38(9):2520-2531.

35. Zhou Y, Cao C, Cao Y, Han Q, Parker CB, Glass JT. Robust and high-performance electrodes via crumpled Au-CNT forests for stretchable supercapacitors. *Matter*. 2020;2(5):1307-1323.

36. Zhou Y, Maleski K, Anasori B, et al. $Ti_3C_2T_x$ Mxene-reduced graphene oxide composite electrodes for stretchable supercapacitor. *ACS Nano*. 2020;14(3):3576-3586.

37. Wang Y, Zhao Y, Han Y, et al. Fixture-free omnidirectional prestretching fabrication and integration of crumpled in-plane micro-supercapacitor. *Sci Adv*. 2022;8(21):eabn8338.

38. Ren Y, Liu Y, Wang S, et al. Stretchable supercapacitor based on a hierarchical PPy/CNT electrode and hybrid hydrogel electrolyte with a wide operating temperature. *Carbon Energy*. 2022;4(4):527-538.

39. Jang S, Min H, Cho SB, et al. A hierarchically tailored wrinkled three-dimensional foam for enhanced elastic supercapacitor electrodes. *Nano Lett*. 2021;21(16):7079-7085.

40. Yang Y, Duan S, Zhao H. Highly conductive silicone elastomers via environment-friendly swelling and in situ synthesis of silver nanoparticles. *Adv Mater Interfaces*. 2021;8(9):2100137.

41. Gao N, Zhang X, Liao S, Jia H, Wang Y. Polymer swelling induced conductive wrinkles for an ultrasensitive pressure sensor. *ACS Macro Lett*. 2016;5(7):823-827.

42. Mo J, Ko Y, Yun YS, Huh J, Cho J. A carbonization/interfacial assembly-driven electroplating approach for water-splitting textile electrodes with remarkably low overpotentials and high operational stability. *Energy Environ Sci*. 2022;15(9):3815-3829.

43. Ko J, Kim D, Song Y, et al. Electroosmosis-driven hydrogel actuators using hydrophobic/hydrophilic layer-by-layer assembly-induced crack electrodes. *ACS Nano*. 2020;14(9):11906-11918.

44. Ko Y, Kwon M, Bae WK, Lee B, Lee SW, Cho J. Flexible supercapacitor electrodes based on real metal-like cellulose papers. *Nat Commun*. 2017;8:536.

45. Woo S, Nam D, Chang W, et al. A layer-by-layer assembly route to electroplated fibril-based 3D porous current collectors for energy storage devices. *Small*. 2021;17(19):2007579.

46. Woehrle GH, Brown LO, Hutchison JE. Thiol-functionalized, 1.5-nm gold nanoparticles through ligand exchange reactions: scope and mechanism of ligand exchange. *J Am Chem Soc*. 2005;127(7):2172-2183.

47. Rumens CV, Ziai MA, Belsey KE, Batchelor JC, Holder SJ. Swelling of PDMS networks in solvent vapours; applications for passive RFID wireless sensors. *J Mater Chem C*. 2015;3(39):10091-10098.

48. Yang S, Khare K, Lin PC. Harnessing surface wrinkle patterns in soft matter. *Adv Funct Mater*. 2010;20(16):2550-2564.

49. Bowden N, Brittain S, Evans AG, Hutchinson JW, Whitesides GM. Spontaneous formation of ordered structures

in thin films of metals supported on an elastomeric polymer. *Nature*. 1998;393(6681):146-149.

50. Ko Y, Lee S, Kwon CH, Lee SW, Cho J. Interfacial design and assembly for flexible energy electrodes with highly efficient energy harvesting, conversion, and storage. *Adv Energy Mater*. 2021;11(27):2002969.

51. Yuan Z, Wang H, Shen J, et al. Hierarchical Cu$_2$S@NiCo-LDH double-shelled nanotube arrays with enhanced electrochemical performance for hybrid supercapacitors. *J Mater Chem A*. 2020;8(42):22163-22174.

52. Zhang G, Hu J, Nie Y, et al. Integrating flexible ultralight 3D Ni micromesh current collector with NiCo bimetallic hydroxide for smart hybrid supercapacitor. *Adv Funct Mater*. 2021;31(24):2100290.

53. Liu Y, Wang Y, Shi C, et al. Co-ZIF derived porous NiCo-LDH nanosheets/N doped carbon foam for high-performance supercapacitor. *Carbon*. 2020;165:129-138.

54. Ko Y, Park J, Mo J, et al. Layer-by-layer assembly-based electrocatalytic fibril electrodes enabling extremely low overpotentials and stable operation at 1 A cm^{-2} in water-splitting reaction. *Adv Funct Mater*. 2021;31(35):2102530.

55. Chodankar NR, Dubal DP, Ji SH, Kim DH. Self-assembled nickel pyrophosphate-decorated amorphous bimetal hydroxides 2D-on-2D nanostructure for high-energy solid-state asymmetric supercapacitor. *Small*. 2019;15(19):1901145.

56. Won Y, Kim A, Yang W, Jeong S, Moon J. A highly stretchable, helical copper nanowire conductor exhibiting a stretchability of 700%. *NPG Asia Mater*. 2014;6:e132.

57. Guo Y, Hong X, Wang Y, et al. Multicomponent hierarchical Cu-doped NiCo-LDH/CuO double arrays for ultralong-life hybrid fiber supercapacitor. *Adv Funct Mater*. 2019; 29(24):1809004.

58. Liu H, Zhu J, Li Z, Shi Z, Zhu J, Mei H. Fe$_2$O$_3$/N doped rGO anode hybridized with NiCo LDH/Co(OH)$_2$ cathode for battery-like supercapacitor. *Chem Eng J*. 2021;403:126325.

59. Wang P, Qi X, Zhao W, Qian M, Bi H, Huang F. Nitrogen-doped hierarchical few-layered porous carbon for efficient electrochemical energy storage. *Carbon Energy*. 2021;3(2): 349-359.

60. Peng H, Yao B, Wei X, et al. Pore and heteroatom engineered carbon foams for supercapacitor. *Adv Energy Mater*. 2019; 9(19):1803665.

61. Augustyn V, Simon P, Dunn B. Pseudocapacitive oxide materials for high-rate electrochemical energy storage. *Energy Environ Sci*. 2014;7(5):1597-1614.

SUPPORTING INFORMATION

Additional supporting information can be found online in the Supporting Information section at the end of this article.